ELSEVIER

Surface Science 445 (2000) 283–299

surface science

www.elsevier.nl/locate/susc

Role of image forces in non-contact scanning force microscope images of ionic surfaces

L.N. Kantorovich, A.S. Foster *, A.L. Shluger, A.M. Stoneham

Department of Physics and Astronomy, University College London, Gower Street, London, WC1E 6BT, UK

Received 20 August 1999; accepted for publication 13 October 1999

Abstract

We consider the effect of the image interaction on the force acting between tip and surface in non-contact scanning force microscope experiments. This interaction is relevant when a conducting tip interacts with either a polar bulk sample or with a thick film grown on a conducting substrate. We compare the atomistic contribution due to the interaction between the microscopic tip apex and the sample with the macroscopic van der Waals and image contributions to the force on the tip for several representative NaCl clusters adsorbed on a metal substrate. We show that the microscopic force dominates above the plain (001) terrace sites and is solely responsible for image contrast. However, the image force becomes comparable to the microscopic force above the surface di-vacancy and dominates the interaction above a charged step. © 2000 Published by Elsevier Science B.V. All rights reserved.

Keywords: AFM; Construction and use of effective interatomic interactions; Insulating films; Metal–insulator interfaces; NaCl; Surface defects

1. Introduction

Although the importance of image interactions has been recognised in metal–insulator interfaces, electrochemistry and other areas, their role in image formation in scanning force microscopy (SFM) has not been analysed in detail [1]. The reasons are mainly related to the small number of experimental situations where these forces were evidently important, e.g. where an ionic insulator would make a contact with a conducting tip. In particular, in most of the SFM applications on insulators, either insulating tips or oxidised Si and metal tips are employed. However, recent applications of scanning tunnelling microscopy (STM) to oxides [2] and insulating films grown on metal substrates [3], and combined applications of STM and non-contact SFM (NC-SFM) (e.g. see Refs. [4–6]) bring these interactions to the forefront. In these applications, conducting tips are interacting with thin polar films grown on metal substrates or with conducting oxides. This means that both the interactions of the tip with the film and of the film with the substrate involve the image force and it should be taken into account in analysis and interpretations of SFM images. Although the same is true for 'contact mode' imaging, in this paper we will focus on a more simple case of NC-SFM in vacuum.

In most NC-SFM setups the cantilever is driven

* Corresponding author. Fax: +44-(0)171-3911360.
E-mail address: adam.foster@ucl.ac.uk (A.S. Foster)

PII: S0039-6028(99)01086-9

with a constant frequency of 100–200 kHz and makes oscillations with an amplitude of about 100–200 Å above the surface [6,7]. When the end of the tip approaches the sample, the main frequency of the cantilever oscillations changes due to the tip–surface interaction. The surface image is obtained as a map of the displacements of the base of the cantilever required to maintain a constant frequency change as the tip scans the surface. Contrast in an image is produced by making displacements away from the surface bright, and those towards it dark. The most stable imaging has been obtained in the attractive region of the tip–surface interaction near the surface. Experimental [7] and theoretical estimates [8] demonstrate that, for stable imaging, the distance between the end of the tip and the surface atoms should be larger than about 4–5 Å. However, these experimental conditions are very difficult to maintain and, in most cases, the tip crashes into the surface many times during one series of experiments [9], but a change of the tip structure during one image is a relatively rare event. Therefore, the structure of the tip apex is dependent not only on vacuum conditions and tip preparation but also on the stability of imaging. Most of the metallic or doped Si tips used in SFM experiments are likely to be covered either by islands of a native oxide and/or by the surface material.

In this paper we consider the relative importance of image forces in NC-SFM contrast formation using the example of a finite cluster of NaCl adsorbed on a metallic substrate. This system has been studied in recent STM [3] and NC-SFM experiments [10,11] and is representative of a common case of an insulating film grown on a metal. First, we describe a numerical method for the effective calculation of the image force between tips and surfaces and its implementation within an atomistic simulation technique. Then we study the relative strength of the image force with respect to the van der Waals and chemical forces in different representative tip–surface systems. These include the surface terrace, neutral and charged steps, and a dipole formed by a vacancy pair at a step. Finally, we discuss the results and limitations of our method.

2. Theory

2.1. Theoretical model

We consider a conducting spherical tip of radius R interacting with a conducting semi-infinite substrate (*substrate*) with an adsorbed finite cluster of ionic material (*sample*) on it (see Fig. 1). To model contamination of a conducting tip by an ionic material, we embed a finite cubic MgO cluster oriented by one of its corners down to the NaCl cluster adsorbed on the metal substrate, as shown in Fig. 1. This model is similar to the one used in Ref. [8], except that now the tip and substrate are conductive. Their conductivity should be enough to keep their surfaces at constant potential at each point of slow cantilever oscillations. The tip and substrate are connected in a joint circuit, as shown in Fig. 1.

Bias applied to the tip and substrate will produce an external non-uniform electrostatic field and an additional contribution to the system energy, which will affect both the geometry of the sample atoms and those of the tip apex, and the force imposed on the tip. However, this effect is not very significant for typical experimental values of the bias (<1 V).

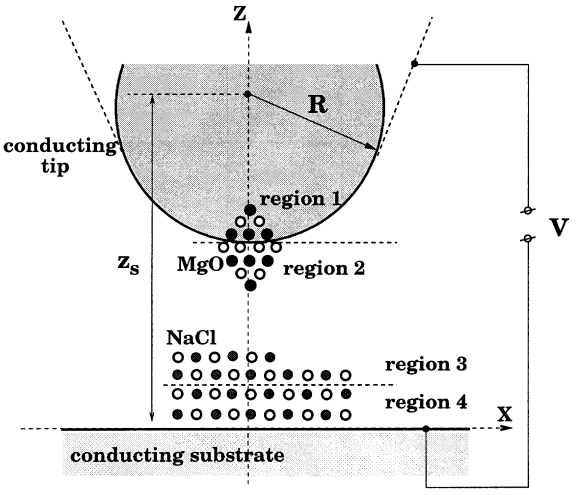

Fig. 1. Schematic picture of the microscopic model used here to simulate the interaction between the tip and the sample. The coordinate axes are aligned with respect to the sphere centre (at $x=y=0$, $z=z_s$) and the metal plane (at $z=0$) for convenience.

Another contribution, which can be more significant for the processes that take place in an SFM experiment, is to do with the *polarisation* of conductive electrodes by the charge density of the sample. The potential on the tip and substrate is maintained by external sources (we shall call them a *battery*). The sample charge density will change this potential. To prevent this from happening, the battery will move some charge between the tip and substrate in order to keep the potential constant. Therefore, there will be some net distribution of charge density on their surfaces that will also interact with the sample and will affect the force imposed on the tip. This kind of induced charge has been commonly referred to as the *image charge* and we will call this interaction the image interaction.

A preliminary account of this effect in application to SFM has been given in Ref. [12], where a simple model example has been considered. Here we present the theoretical microscopic model in detail and propose an efficient method that can be used to take this effect into account in a systematic manner. Note that quantum effects in metal polarisation [13–16] are neglected here and our consideration is based entirely on classical electrostatics. According to this model, the image charge does not penetrate into the bulk of the metal. In reality, however, there is some distribution of the charge inside the metals [13–15]. However, this effect is not important for processes that occur at distances of the order of several Ångströms outside the metal and, therefore, will be neglected in this study.

All the atoms comprising the microscopic part of the system are split into three regions, as shown schematically in Fig. 1. The tip apex is modelled by a cluster that is formally divided into two regions. The atoms in region 2 are allowed to adjust their positions, whereas atoms in region 1 are kept fixed in order to keep the shape of the apex. The atoms in region 1 move together with the macroscopic part of the tip and, therefore, their positions are determined only by the tip position along the vertical z-axes, which we will denote z_s. Atoms in region 2 follow the tip as well, since they are strongly bound to the atoms in region 1. However, their positions can change appreciably due to the tip–surface interaction. Finally, the sample atoms in region 3 are also allowed to relax, except in the two layers closest to the substrate (region 4). The interactions between atoms in regions 1 to 4 are calculated using semi-empirical interatomic potentials and the shell model to treat atomic polarisabilities. Details of these calculations are given in Section 3.1.

In order to calculate the force imposed on the tip we used the following expression for the total energy of the system:

$$U=\tfrac{1}{2}\sum_{ij}{}' v_{ij}+U_{\mathrm{vdW}}+U_{\mathrm{el}}, \tag{1}$$

where v_{ij} is the interatomic potential between atoms i, j in regions 1 to 4. This interaction energy is a function of both the tip position z_s and the coordinates $\boldsymbol{r}_i$ of all atoms (and shells) involved. The energy U_{vdW} represents the van der Waals interaction between the macroscopic tip and substrate and depends only on the tip height z_s with respect to the substrate (see Fig. 1). Note that in the present model the macroscopic van der Waals interaction does not affect atomic positions in regions 1 to 4.

The last term in Eq. (1) represents the total electrostatic energy of the whole system. We assume that the Coulomb interaction between all atoms in regions 1–4 is included in the first term in Eq. (1) and hence should be excluded from U_{el}. Therefore, the energy U_{el} includes the interaction of the atoms in the system with the macroscopic tip and substrate. As has been demonstrated in Ref. [12], the correct electrostatic energy should incorporate the work done by the battery to maintain the constant potential on the electrodes. This can be written in the following form [12]:

$$U_{\mathrm{el}}=-\tfrac{1}{2}\,Q^{(0)}V+\sum_{1} q_i\phi^{(0)}(\boldsymbol{r}_i)+\tfrac{1}{2}\sum_{i,j} q_i q_j \phi_{\mathrm{ind}}(\boldsymbol{r}_i,\boldsymbol{r}_j). \tag{2}$$

Here V is the potential difference applied to the metal electrodes. In the setup shown in Fig. 1, without loss of generality [12], one can choose the potential ϕ on the metal plane to be zero, so that the potential on the macroscopic part of the tip

will be $\phi = V$. We also note that the substrate is considered in the limit of a sphere of a very big radius $R' \gg R$, since the metal electrodes formally cannot be infinite [12]. The charge on the tip *without* charges outside the metals (i.e. when there are only bare electrodes and the polarization effects can be neglected) is $Q^{(0)}$ and the electrostatic potential of the bare electrodes anywhere outside the metals is $\phi^{(0)}(\boldsymbol{r})$. The charge $Q^{(0)}$ and the potential $\phi^{(0)}(\boldsymbol{r})$ depend only on the geometry of the capacitor formed by the two electrodes and on the bias V. The charge $Q^{(0)}$ can be calculated from the potential $\phi^{(0)}(\boldsymbol{r})$ as follows [17]:

$$Q^{(0)} = -\frac{1}{4\pi}\int\int \frac{\partial \phi^{(0)}}{\partial n}\,\mathrm{d}s,$$

where the integration is performed over the entire surface of the macroscopic part of the tip with the integrand being the normal derivative of the potential $\phi^{(0)}(\boldsymbol{r})$; the normal $\boldsymbol{n}$ is directed outside the metal. Summation in the second term of Eq. (2) is performed over the atoms and shells of the sample and those of the tip apex that are represented by point charges q_i at positions $\boldsymbol{r}_i$. Note that only those atoms and shells of regions 2–4 are considered explicitly in the energy U_{el} and included in the summation in Eq. (2) (see Section 3.1).

Finally, $\phi_{\mathrm{ind}}(\boldsymbol{r}, \boldsymbol{r}')$ in Eq. (2) is the potential at $\boldsymbol{r}$ due to image charges *induced* on all the metals by a unit point charge at $\boldsymbol{r}'$. This function is directly related to the Green function $G(\boldsymbol{r}, \boldsymbol{r}')$ of the Laplace equation, $\phi_{\mathrm{ind}}(\boldsymbol{r}, \boldsymbol{r}') = G(\boldsymbol{r}, \boldsymbol{r}') - (1/|\boldsymbol{r}, \boldsymbol{r}'|)$, and is symmetric [12], i.e. $\phi_{\mathrm{ind}}(\boldsymbol{r}, \boldsymbol{r}') = \phi_{\mathrm{ind}}(\boldsymbol{r}', \boldsymbol{r})$, due to the symmetry of the Green function itself [18]. The total potential at $\boldsymbol{r}$ due to a net charge induced on all conductors present in the system by all the point charges $\{q_i\}$:

$$\phi_{\mathrm{ind}}(\boldsymbol{r}) = \sum_i q_i \phi_{\mathrm{ind}}(\boldsymbol{r}, \boldsymbol{r}_i) \tag{3}$$

is the *image potential*. Note that the last double summation in Eq. (2) includes the $i=j$ term as well. This term corresponds to the interaction of the charge q_i with its own polarisation (similar to the polaronic effect in solid-state physics).

The function $\phi_{\mathrm{ind}}(\boldsymbol{r}, \boldsymbol{r}')$ and, therefore, the image, $\phi_{\mathrm{ind}}(\boldsymbol{r})$, together with the potential $\phi^{(0)}(\boldsymbol{r})$ of the bare electrodes could be calculated [12] if we knew the exact Green function of the electrostatic problem

$$\Delta_{r'} G(\boldsymbol{r}, \boldsymbol{r}') = -4\pi\delta(\boldsymbol{r} - \boldsymbol{r}') \tag{4}$$

with the corresponding boundary conditions [$G(\boldsymbol{r}, \boldsymbol{r}') = 0$ when $\boldsymbol{r}$ or $\boldsymbol{r}'$ belong to either the substrate or the tip surface] [18]. Therefore, given the applied bias V, the geometric characteristics of the capacitor and the positions $\{\boldsymbol{r}_j\}$ of the point charges $\{q_i\}$ between the tip and sample, one can calculate the electrostatic energy U_{el}. The problem is that the Green function for real tip–sample shapes and arrangements is difficult to calculate. However, for a number of simple geometries, exact solutions of the corresponding electrostatic problems exist. The most common is the planar–planar geometry [19–22], although some non-planar geometries have also been considered, for example a planar–hyperboloidal [22,23], a planar–spherical [24] and a planar–planar junction with a spherical boss at one of the electrodes [25,26].

In this study we use the planar–spherical geometry of the junction, as depicted in Fig. 1. Although a similar model has already been considered in Ref. [24], no details were given and the authors of the cited paper claimed that the method of multiple images that they used did not give a well-converged expansion. Therefore, in Section 2.2 we give a brief description of our method, which is also based on the method of multiple images, together with some details that will be important later to derive the forces acting on the charges and on the tip. Our method appears to be more efficient than the one applied in Ref. [24], as we sum the series of image charges explicitly only for a small number of the first terms, whereas the rest of the series is summed analytically up to infinity. Note that a similar idea was employed in Ref. [20], where the rest of the series of image charges for the planar–planar junction was integrated.

2.2. Solution of the electrostatic problem of point charges inside the sphere–plane capacitor

First, let us consider the calculation of the potential $\phi^{(0)}(\boldsymbol{r})$ of the bare electrodes, i.e. the capacitor problem. We note that the potential $\phi^{(0)}(\boldsymbol{r})$ satisfies the same boundary conditions as

the original problem, i.e. $\phi^{(0)}=0$ and $\phi^{(0)}=-V$ at the lower and upper electrodes respectively. The solution for the plane–spherical capacitor is well known [19] and can be given using the method of image charges (see also Ref. [12]). Since we will need this solution for calculating forces later on, we have to give it here in detail. It is convenient to choose the coordinate system as shown in Fig. 1. Then it is easy to check that the following two *infinite* sequences of image charges give the potential at the sphere and the metal planes as V and zero respectively. The first sequence is given by the image charges $\varsigma_1=RV$ and then $\varsigma_{k+1}=\varsigma_k/D_k$ for $\forall k=1, 2, \ldots$, where the dimensionless constants D_k are defined by the recurrence relation $D_{k+1}=2\lambda-(1/D_k)$ with $D_1=2\lambda$ and $\lambda=z_s/R>1$, z_s being the distance between the sphere centre and the plane (Fig. 1). The point charges $\{\varsigma_k\}$ are all inside the sphere along the normal line passing through the sphere centre. Their z-coordinates are as follows: $z_1=z_s$ and $z_{k+1}=R[\lambda-(1/D_k)]=R(D_k+1-\lambda)$ for $\forall k=1, 2, \ldots$. The second sequence of charges $\{\varsigma_k'\}$ is formed by the images of the first sequence with respect to the metal plane, i.e. $\varsigma_k'=-\varsigma_k$ and $z_k'=-z_k$. An interesting point about the images charges $\{\varsigma_k\}$ is that they converge very quickly at the point $z_\infty=R\sqrt{\lambda^2-1}$ (i.e. $z_k\to\infty$ with $k\to\infty$) and that $z_{k+1}<z_k\ \forall k$. This is because the numbers D_k converge rapidly to the limiting value $D_\infty=\lambda+\sqrt{\lambda^2-1}$, which follows from the original recurrent relation above, $D_\infty=2\lambda-(1/D_\infty)$. Therefore, while calculating the potential $\phi^{(0)}(\boldsymbol{r})$, one can consider the charges $\{\varsigma_k\}$ and $\{\varsigma_k'\}$ explicitly only up to some $k=k_0-1$ and then sum up the rest of the charges to infinity analytically to obtain the effective charge

$$\varsigma_\infty=\sum_{k=k_0}^{\infty}\varsigma_k=\sum_{n=0}^{\infty}\frac{\varsigma_{k_0}}{D_\infty^n}=\frac{\varsigma_{k_0}D_\infty}{D_\infty-1}$$

to be placed at z_∞. This can be used *instead* of the rest of the series:

$$\phi^{(0)}(\boldsymbol{r})=\sum_{k=1}^{k_0}\bar{\varsigma}_k\left(\frac{1}{|\boldsymbol{r}-\boldsymbol{r}_{\varsigma_k}|}-\frac{1}{|\boldsymbol{r}-\hat{\sigma}\boldsymbol{r}_{\varsigma_k}|}\right), \tag{5}$$

where $\bar{\varsigma}_k=\varsigma_k$ for $k<k_0$ and $\bar{\varsigma}_{k_0}=\varsigma_\infty$; then, $\boldsymbol{r}_{\varsigma_k}=(0, 0, z_k)$ is the position vector of the charge ς_k and $\boldsymbol{r}_{\varsigma_k}'=\hat{\sigma}\boldsymbol{r}_{\varsigma_k}=(0, 0, -z_k)$ is the position of the charge ς_k' ($\hat{\sigma}$ means reflection with respect to the substrate surface $z=0$). To find the charge $Q^{(0)}$, which is also needed for the calculation of the electrostatic energy, Eq. (2), one should calculate the normal derivative of the potential $\phi^{(0)}(\boldsymbol{r})$ on the sphere and then take the corresponding surface integral (see above). However, it is useful to recall that the total charge induced on the metal sphere due to an external charge is equal exactly to the image charge inside the sphere [17,18]. Therefore, one immediately obtains:

$$Q^{(0)}=\sum_{k=1}^{k_0}\bar{\varsigma}_k. \tag{6}$$

Note that the potential $\phi^{(0)}(\boldsymbol{r})$ and the charge $Q^{(0)}$ depend on the position z_s of the sphere *indirectly* via the charges ς_k and their positions $\boldsymbol{r}_{\varsigma_k}$ according to the recurrent expressions above. Therefore, one has to be careful when calculating the contribution to the force imposed on the tip due to bias V [i.e. when differentiating $\phi^{(0)}(\boldsymbol{r})$ and $Q^{(0)}$ in Eq. (2)].

Now we turn to the calculation of the function $\phi_{\mathrm{ind}}(\boldsymbol{r}, \boldsymbol{r}')$ in Eq. (2). This function corresponds to the image potential at a point $\boldsymbol{r}$ due to a unit charge at $\boldsymbol{r}'$. This potential is to be defined in such a way that, together with the direct potential of the unit point charge, it should be zero on both electrodes (the boundary conditions for the Green function). Thus, let us consider a unit charge $q=1$ at $\boldsymbol{r}_q$ somewhere outside the metal electrodes, as shown in Fig. 2. We first create the direct image $-q$ of this charge with respect to the plane at the point $\boldsymbol{r}_q'=\hat{\sigma}\boldsymbol{r}_q$ to maintain zero potential at the plane. Then, we create images of the two charges, $q=1$ and $-q=-1$, with respect to the sphere to get two image charges $\xi_1=-R/|r_q-R_s|$ and $\zeta_1=R/|\hat{\sigma}\boldsymbol{r}_q-R_s|$, as shown in Fig. 2, where $\boldsymbol{R}_s=(0, 0, z_s)$. These image charges are both inside the sphere by construction and their positions can be written down using a vector function $\boldsymbol{f}(\boldsymbol{r})=\boldsymbol{R}_s+R^2[(\boldsymbol{r}-\boldsymbol{R}_s)/|\boldsymbol{r}-\boldsymbol{R}_s|^2]$ as follows: $\boldsymbol{r}_{\xi_1}=\boldsymbol{f}(\boldsymbol{r}_q)$ and $\boldsymbol{r}_{\varsigma_1}=\boldsymbol{f}(\hat{\sigma}\boldsymbol{r}_q)$. Now the potential at the surface will be zero. At the next step we construct the images $\xi_1'=-\xi_1$ and $\zeta_1'=-\zeta_1$ of the charges ξ_1 and ζ_1 in the plane, at points $\hat{\sigma}\boldsymbol{r}_{\xi_1}$ and $\hat{\sigma}\boldsymbol{r}_{\zeta_1}$ respectively, to get the potential at the plane also zero. This process is continued, and in this way two infinite sequences of image charges are

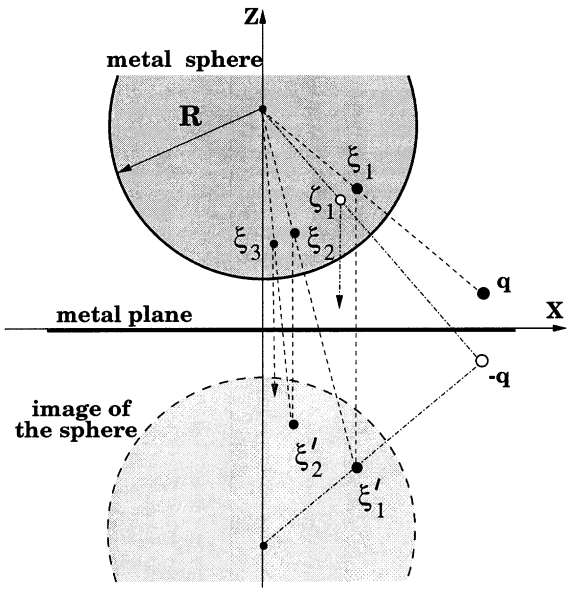

Fig. 2. Construction of image charges in the sphere–plane capacitor system due to one charge q outside the metals.

constructed, which are given by the following recurrence relations:

$$\xi_{k+1}=\xi_k\frac{R}{|\hat{\sigma}\boldsymbol{r}_{\xi_k}-\boldsymbol{R}_s|}$$

$$\boldsymbol{r}_{\zeta_{k+1}}=\boldsymbol{f}(\hat{\sigma}\boldsymbol{r}_{\xi_k})=\boldsymbol{R}_s+R^2\frac{\hat{\sigma}\boldsymbol{r}_{\xi_k}-\boldsymbol{R}_s}{|\hat{\sigma}\boldsymbol{r}_{\xi_k}-\boldsymbol{R}_s|^2}, \tag{7}$$

where $k=1, 2, \ldots$ and similarly for the ζ-sequence. Note, however, that the two sequences start from different initial charges. Namely, the ξ-sequence starts from the original charge q and the ζ-sequence from its image in the plane $-q$. The two sequences $\{\xi_k\}$ and $\{\zeta_k\}$ are to be accompanied by the other two sequences $\{\xi'_k\}$ and $\{\zeta'_k\}$, which are the images of the former charges with respect to the plane. The four sequences of the image charges and the charges q and $-q$ provide the correct solution for the problem formulated above since they produce the potential that is the solution of the corresponding Poisson equation and, at the same time, is zero both on the metal sphere and the metal plane.

It is useful to study the convergence properties of the sequences of image charges. To simplify the notation, let us assume that the original charge is in the xz-plane. Then it follows from Eq. (7) that $x_{\xi_{k+1}}<x_{\xi_k}$. It is also seen that $x_{\xi_k}\to 0$ and $z_{\xi_k}\to z_\infty=R\sqrt{\lambda^2-1}$ (see above) as $k\to\infty$ and the same for the ζ-sequence. This means that the image charges inside the sphere move towards the vertical line passing through the centre of the sphere and finally converge at the same point z_∞. This is the same behaviour we observed for charges in the capacitor problem at the beginning of this section (see Fig. 2). In fact, the calculation clearly shows a very fast convergence, so that we can again sum up the series of charges from $k=k_0$. Thus, the image potential at a point $\boldsymbol{r}$ due to the unit charge at $\boldsymbol{r}_q$ is:

$$\phi_{\rm ind}(\boldsymbol{r},\boldsymbol{r}_q)=-\frac{1}{\boldsymbol{r}-\hat{\sigma}\boldsymbol{r}_q}+\sum_{k=1}^{k_0}\left[\bar{\xi}_k\left(\frac{1}{|\boldsymbol{r}-\boldsymbol{r}_{\xi_k}|}-\frac{1}{|\boldsymbol{r}-\hat{\sigma}\boldsymbol{r}_{\xi_k}|}\right)+\bar{\zeta}_k\left(\frac{1}{|\boldsymbol{r}-\boldsymbol{r}_{\zeta_k}|}-\frac{1}{|\boldsymbol{r}-\hat{\sigma}\boldsymbol{r}_{\zeta_k}|}\right)\right], \tag{8}$$

where $\bar{\xi}_k=\xi_k$ for $k<k_0$ and $\bar{\xi}_{k_0}=\xi_\infty=\xi_{k_0}(D_\infty/D_\infty-1)$, and similarly for the ζ-sequence. Here D_∞ is the geometrical characteristic of the capacitor introduced at the beginning of this section.

As has already been mentioned in Section 2.1, the function $\phi_{\rm ind}(\boldsymbol{r},\boldsymbol{r}_q)$ must be symmetric with respect to the permutation of its two variables. It is not at all obvious that this is the case, since the meaning of its two arguments in Eq. (8) is rather different. Nevertheless, we show in Appendix A that the function $\phi_{\rm ind}(\boldsymbol{r},\boldsymbol{r}_q)$ is symmetric.

2.3. The calculation of the total force acting on the tip

In order to calculate the total force acting on the tip, one has to differentiate the total energy, Eq. (1), with respect to the position of the sphere $\boldsymbol{R}_s$. Since we are interested only in the force acting in the z-direction, it is sufficient to study the dependence of the energy on z_s. There will be three contributions to the force. The force from the electrostatic energy is considered in some detail in Appendix B. The second contribution to the force comes from the van der Waals interaction [27].

Finally, the interatomic interactions in regions 1–4 lead to a force that is calculated by differentiating the shell-model energy [the first term in Eq. (1)]. Therefore:

$$F_{\rm tip} = -\frac{{\rm d}U_{\rm sh}}{{\rm d}z_{\rm s}} - \frac{{\rm d}U_{\rm vdW}}{{\rm d}z_{\rm s}} - \frac{{\rm d}U_{\rm el}}{{\rm d}z_{\rm s}}, \tag{9}$$

where $U_{\rm sh} = \frac{1}{2}\Sigma_{ij}\,'v_{ij}$ is the shell model energy. We recall that the summation here is performed over all atoms in regions 1 to 4. Only positions of the atoms in region 1 depend directly on $z_{\rm s}$, since atoms in regions 2 and 3 are allowed to relax. However, their equilibrium positions, $\boldsymbol{r}_i^{(0)}$, determined by the minimisation of the energy of Eq. (1), will depend *indirectly* on $z_{\rm s}$ at equilibrium, $\boldsymbol{r}_i^{(0)} = \boldsymbol{r}_i^{(0)}(z_{\rm s})$. Then, we also recall that the electrostatic energy $U_{\rm el}$ depends only on positions of atoms in regions 2 to 4, as well as on the tip position $z_{\rm s}$.

Let us denote the positions of atoms in regions 2 to 4 by a vector $\boldsymbol{x} = (\boldsymbol{r}_1, \boldsymbol{r}_2, \ldots)$. The total energy $U = U(\boldsymbol{x}, z_{\rm s})$, where the direct dependence on $z_{\rm s}$ comes from atoms in region 1 of the shell model energy $U_{\rm sh}$ and from the electrostatic energy $U_{\rm el}$. In equilibrium the total energy is a minimum:

$$\left(\frac{\partial U}{\partial \boldsymbol{x}}\right)_{z_{\rm s}} = 0, \tag{10}$$

where the derivatives are calculated at a given fixed tip position $z_{\rm s}$. Let $\boldsymbol{x}_0 = (\boldsymbol{r}_1^{(0)}, \boldsymbol{r}_2^{(0)}, \ldots)$ be the solution of Eq. (10). Then, since $\boldsymbol{x}_0 = \boldsymbol{x}_0(z_{\rm s})$, we have for the force:

$$F_{\rm tip} = -\frac{{\rm d}U[\boldsymbol{x}_0(z_{\rm s}), z_{\rm s}]}{{\rm d}z_{\rm s}} = -\left(\frac{\partial U}{\partial \boldsymbol{x}_0}\right)_{z_{\rm s}} \frac{\partial \boldsymbol{x}_0}{\partial z_{\rm s}} - \left(\frac{\partial U}{\partial z_{\rm s}}\right)_{x_0} = -\left(\frac{\partial U}{\partial z_{\rm s}}\right)_{x_0}, \tag{11}$$

where we have used Eq. (10). This result can be simplified further. Indeed, the partial derivative of the shell-model, $-(\partial U_{\rm sh}/\partial z_{\rm s})$, is equal to the sum of all z-forces acting on atoms in region 1 due to all shell-model interactions, since only these atoms are responsible for the dependence on $z_{\rm s}$ in the energy $U_{\rm sh}$. Therefore, finally we have:

$$F_{\rm tip} = \sum_{i\in 1} [F_{iz}^{\rm (sh)}]_{x_0} - \frac{{\rm d}U_{\rm vdW}}{{\rm d}z_{\rm s}} - \left(\frac{\partial U_{\rm el}}{\partial z_{\rm s}}\right)_{x_0}, \tag{12}$$

where the first summation runs only over atoms in region 1. Thus, in order to calculate the force imposed on the tip at a given tip position $z_{\rm s}$, one has to relax the positions of atoms in regions 2 and 3 using the *total energy* of the system, $U_{\rm sh} + U_{\rm el}$. Then one calculates the shell-model force, $F_{iz}^{\rm (sh)}$, acting on every atom in region 1 in the z-direction as well as the electrostatic contribution to the force given by the last term in Eq. (12). The van der Waals force between the macroscopic tip and sample does not depend on the geometry of the atoms and can be calculated just once for every given $z_{\rm s}$.

Although the expression for the force obtained above is exact for the model used in this study, such a calculation is quite demanding since it requires using the electrostatic energy $U_{\rm el}$ alongside with the shell-model energy $U_{\rm sh}$ in the optimisation process. Most time is spent in the calculation of the forces imposed on atoms due to the energy $U_{\rm el}$. Therefore, in this work we have adopted the following approximate strategy. For every tip position, all atoms in regions 2 and 3 were allowed to relax to mechanical equilibrium in accordance with the shell-model interactions only and we neglected the effect of the image charges on their geometry. To investigate the effect of this, we performed some fully self-consistent calculations in the NaCl step system. In these calculations, ions in regions 2 and 3 are allowed to relax completely with respect to microscopic *and image forces*. We found that the displacements of ions in the system due to image forces was less than 0.01 Å and would not affect our results.

The force acting on the tip was calculated using an equation similar to Eq. (12):

$$F_{\rm tip} \simeq \sum_{i\in 1} [F_{iz}^{\rm (sh)}]_{x_0} + \sum_{i\in 2} [F_{iz}^{\rm (el)}]_{x_0} - \frac{{\rm d}U_{\rm vdW}}{{\rm d}z_{\rm s}} - \left(\frac{\partial U_{\rm el}}{\partial z_{\rm s}}\right)_{x_0}, \tag{13}$$

where in the second summation we sum all z-forces acting on all atoms of region 2 due to the

electrostatic energy U_{el}. The calculation of the electrostatic contribution to the forces acting on atoms is considered in detail in Appendix C.

3. Results

In order to demonstrate the relative significance of the image force with respect to the other forces, we applied the interaction model described above to calculate the tip–surface forces of several characteristic systems. These systems were chosen as they represent a surface–substrate class that has been studied extensively in STM [3] and NC-SFM experiments [10,11]. Specifically, each of the systems represents a feature that is likely to be found in experiment, and in which image forces may play a significant role in the interactions.

3.1. Details of the calculations

The systems used to calculate the forces are all set up as shown in Fig. 1, with only the exact structure of the NaCl cluster changing between systems. For these calculations the tip consists of a sphere of radius 100 Å with a 64-atom MgO cube embedded at the apex. The cube is orientated so that it is symmetric about the z-axis with a single oxygen ion at the lowest point of the tip. The top three layers of the cube fall within the sphere's radius and constitute region 1, as shown in Fig. 1. The exact number of ions in region 1 is set so as to keep the nano-tip attached to the sphere neutral. The remaining ions of the cube constitute region 2. The clusters used consist of four layers of NaCl, with the top two layers designated region 3 and the bottom two layers region 4, as in Fig. 1. The metal plate is 2 Å below the bottom of the cluster and the bias is held at 1.0 V in all calculations. This setup is consistent through all systems calculated and, where appropriate, for all interactions calculated. This gives us confidence that we can compare the relative values of forces in the same system and between different systems.

The interaction between ions in regions 1–4 was calculated using a static atomistic simulation technique as implemented in the MARVIN computer code [28,29]. We will refer to this interaction as *microscopic* in further discussion. The nano-tip and the NaCl cluster are each divided into two regions, I and II. In terms of Fig. 1, region I consists of region 2 and the top two layers of the cluster (region 3), and region II consists of region 1 and the remaining bottom two layers of the cluster (region 4). The region I ions are relaxed explicitly, whilst the region II ions are kept fixed to reproduce the potential of the bulk lattice and the remaining tip ions in the relaxed ions. The calculation is periodic, so that the infinite surface is represented; however, this means large surface unit cells must be used to avoid interactions between tip images in different cells. We made sure that the shell-model contribution to the force is completely converged with respect to the size of the periodically translated simulation cell.

Electronic polarisation of the ions is implemented via the Dick–Overhauser shell model [30]. Buckingham two-body potentials were used to represent the non-coulombic interactions between the ions. The parameters for these interactions are well tested and are fully described in Ref. [31]. To calculate the shell-model contribution to the microscopic force between tip and surface, $\Sigma_{i\in 1}\,[F_{iz}^{(sm)}]_{x_0}$ [see Eq. (13)], we first calculate the total shell-model energy of the system at a range of tip–surface separations, and then differentiate it numerically to find the force as a function of separation.

The image force is calculated by taking the relaxed geometry from the shell-model calculation at each tip–surface separation. Any ions within the sphere (i.e. region 1) are not considered in the image force calculation, as it is impossible to have ions within the conducting sphere. Also, any ions closer than 2.5 Å to the sphere did not produce any images within the sphere, as these would produce an unrealistically large interaction. The force on each atom in the system due to the image interaction is then calculated, and the force on the tip atoms is summed to find the contribution of the image force to the tip–surface force, see Eq. (13). This calculation is not periodic; the NaCl cluster is now a finite body. However, since our NaCl periodic cell is large enough that we can neglect the interaction between the tip images, we

can effectively consider the NaCl sample to be a finite cluster at all stages of the calculation. The only difference is that the periodic boundary conditions in atomistic simulations do not allow the atoms at the cluster border to relax as in a free cluster. However, this effect is small and does not affect our conclusions. The approach described allows us to ensure the consistency of our model shown in Fig. 1 throughout the whole modelling process.

The final contribution to the force is the van der Waals interaction. It includes the following contributions: (i) between the macroscopic Si tip of conical shape with the sphere of radius R at the end [27] and semi-infinite substrate; (ii) the dispersion forces between the atoms in the sample treated atomistically; and (iii) the interaction between the macroscopic part of the tip and the sample atoms. The first contribution is calculated analytically [27]. In fact, the macroscopic contribution to the van der Waals force is the same in each of the three systems described below, as it depends only on the tip–surface separation, macroscopic sphere radius, cone-angle and Hamaker constant of the system [27]. All these quantities are identical in each system we look at, so that the van der Waals force acts as a background attractive force independent of the microscopic properties of the system [8]. The Hamaker constant needed for the calculation of the macroscopic van der Waals force is estimated to be 0.5 eV [32].

To estimate the importance of the third contribution, we have calculated explicitly the dispersion interaction between one atom and a spherical block of atoms. We found that this interaction converges to a constant value when the radius of the sphere exceeds about 30 Å. The force exerted on one atom due to this interaction at characteristic tip–sample distances is several orders of magnitude smaller than the force between macroscopic tip and substrate. Also, the force decays with distance as r^{-4}. This effectively means that only the top layer of the sample contributes to the van der Waals force, and there are not enough ions in that layer for it to be significant. Therefore, we neglected this interaction in further calculations.

3.2. NaCl step

The first system studied was a stepped NaCl cluster produced by placing a $5\times3\times2$ (in terms of an eight-atom cubic unit cell) block on top of a $5\times5\times2$ block so that two corners are aligned. A schematic for the calculation cell of this system is shown in Fig. 3. This system gives us a good opportunity to study the interactions over sites of different coordination. The upper terrace of the step is a good representation of the ideal (001) surface of NaCl; as long as we remain at least three rows from the edge the forces are converged with respect to row choice. However, the ions of the step-edge have a coordination of four, compared with a coordination of five for the terrace ions.

To study the difference between these types of site we calculated the interactions over an Na ion in the terrace and a Cl ion at the step edge, as

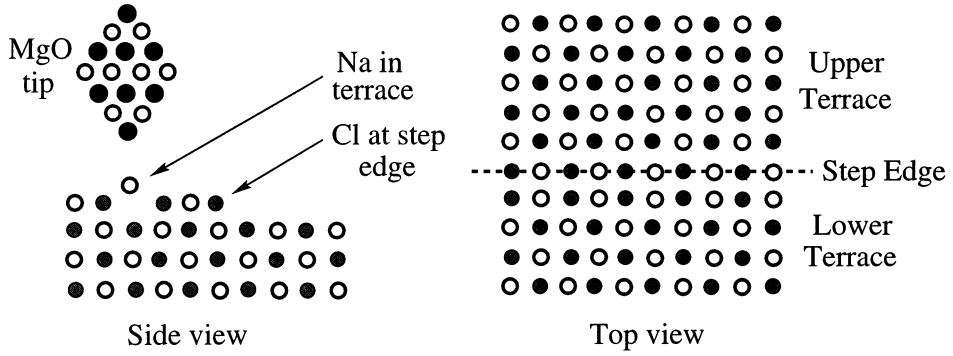

Fig. 3. System schematic for NaCl step.

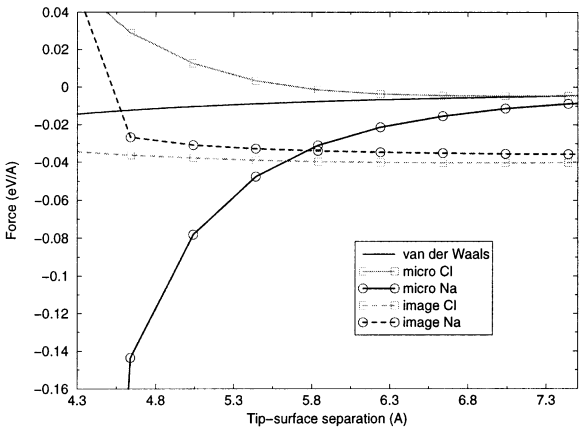

Fig. 4. Forces over NaCl step.

shown in Fig. 3. This allows us to compare the effects of coordination and chemical identity with the forces between tip and surface.

The first point to note is that the macroscopic van der Waals force is the same for both anion and cation; this is an obvious effect from the way in which we calculate this interaction. It is also the least significant force at tip–surface separations less than 6 Å, as can be seen in Fig. 4.

The behaviour of the microscopic force is as would be expected for the interaction of an oxygen ion (which simulates the end of the tip apex, see above) with the ions in the surface. The force is attractive over the positive Na in the terrace and repulsive over the negative Cl at the step edge. The microscopic force becomes the dominant interaction in the system at around 5.5 Å. As the tip gets very close to the Na ion in the terrace the ion begins to displace towards the tip oxygen, greatly increasing the attractive force. When the separation is closer than around 4.7 Å the displacement of the Na ion towards the tip exceeds 1 Å. This ion instability can be seen clearly both in the microscopic and image force curves for Na in Fig. 4 and has already been described in the literature in the context of AFM [33].

The image force itself is the dominant interaction at longer ranges, but it is fairly consistent over cation and anion in the NaCl terrace. The difference in image force over the Cl and Na ions is less than 0.01 eV/Å until the instability at 4.7 Å. This means that for this system the image force acts in a similar way to the macroscopic van der Waals force, i.e. as an attractive background force that is blind to atomic identity and, therefore, does not contribute to the SFM image contrast.

3.3. Pair vacancy

The second system studied is formed by taking the NaCl step discussed in Section 3.2 and removing an Na–Cl pair of nearest-neighbour ions from the upper terrace, as shown in Fig. 5. This effectively creates a dipole on the upper terrace of the step, but does not greatly affect the original geometry of the step.

In this system we calculated the total force contributions over the ions at the edge of the pair vacancy: the Na ion labelled 1 in Fig. 5 and Cl ion labelled 2. The force contributions as a function of tip–surface separation are shown in Fig. 6. The macroscopic van der Waals force is obviously identical to the previous example, and is here only for comparison. The microscopic force is also very similar to the previous example. This is expected, as we are still looking at the interaction over the same ions and the double vacancy of oppositely charged ions has little significant effect on this force. The removal of the vacancy ions does change the local coordination of the ions at the edge of the vacancy, but this is compensated by relaxation of these ions away from the vacancy. This compensation means that the microscopic van der Waals and electrostatic force directly over the edge ions are similar to the force over the ions in the defect-

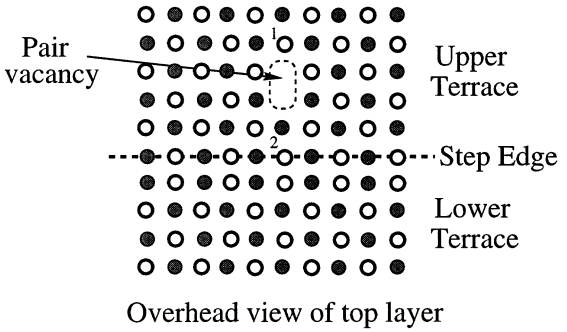

Fig. 5. System schematic for pair vacancy on NaCl terrace.

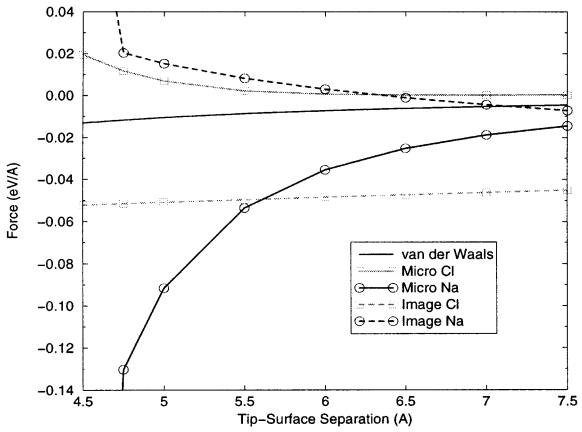

Fig. 6. Forces over pair vacancy in NaCl step.

free terrace. This is seen clearly by the onset of Na ion instability at the same tip–surface separation of about 4.7 Å.

The image force over the edge ions demonstrates very different behaviour to the plain step system studied in Section 3.2. The only similarity is that the microscopic force becomes the dominant interaction at the same distance of 5.5 Å. The image force over the Cl vacancy edge ion is attractive and almost twice as large (-0.05 eV/Å) as the force over the Cl at the plain step edge (-0.03 eV/Å). The image force clearly feels the defect in the terrace and the increase in force reflects the change in the local charge environment of the Cl ion. This is even more clearly shown by the image force over the Na ion at the vacancy edge. The force is much smaller than the microscopic force at all separations and actually becomes repulsive at around 6.2 Å. This means that the induced potential in the conducting tip reflects the change in local charge environment produced by the vacancy. The net interaction over the Cl ion is attractive and repulsive over the Na ion. The difference in magnitude of the image force over the two ions is due to the asymmetry of the nano-tip ions at the end of the conducting tip. Although this result implies that the image force is somewhat sensitive to the geometry of the interacting feature, it does demonstrate that the image force would feel a defect in the surface.

3.4. Charged step

In the final system studied, we looked at a charged step where *similar* ions run along each edge of the step. Fig. 7 shows a schematic of the calculation cell used. The system is created by taking the neutral step setup from Section 3.2 and just removing ions from four rows of the upper terrace. This charged row of ions is similar to the bridging oxygen rows seen in the TiO_2 (110) surface, a surface that has recently been studied experimentally by NC-SFM [34].

We calculated the contributions to the total force over a Cl ion at one edge of the step, labelled 1 in Fig. 7, and over an Na ion at the other edge, labelled 2. The force contributions are shown in Fig. 8.

The macroscopic van der Waals force for the charged step is again identical to previous examples and plotted only for comparison. The microscopic van der Waals and electrostatic forces over both the ions are increased compared with the previous two systems. Over the Na ion at the step edge the force is -0.1 eV/Å at 5.5 Å compared with -0.05 eV/Å at 5.5 Å for the Na ion in the terrace of the plain step. This doubling of the force is also seen over the Cl ion, where the force at 5.5 Å is 0.025 eV/Å over the charged step and 0.012 eV/Å over the plain step. This is a consequence of the

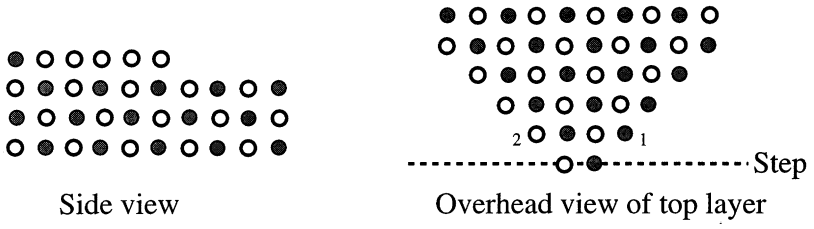

Fig. 7. System schematic for charged NaCl step.

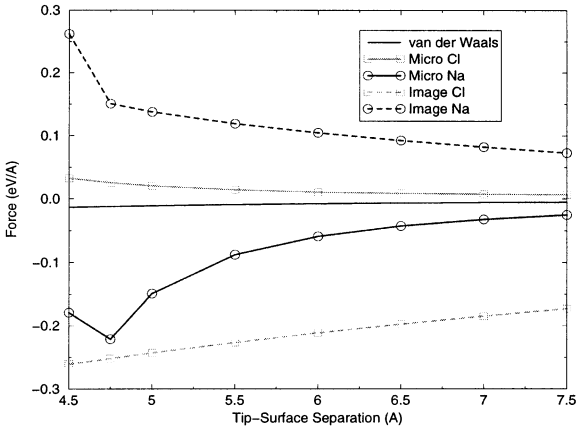

Fig. 8. Forces over charged NaCl step.

change of geometry of the charged step system: both ions have lower coordination than the ions in the plain step system. Lowering the coordination increases the gradient of the electrostatic potential around these ions and, therefore, increases the microscopic force between tip and surface.

The image force dominates the interactions over the charged step at nearly all tip–surface separations; only after the onset of Na ion instability at 4.7 Å does the microscopic attraction between the tip and the step Na overcome the image force. Over the Cl ion the image force is completely dominant, and is approximately an order of magnitude larger than the microscopic force. At the edge of the charged step, the row of similar ions produces a row of similar image charges of opposite sign in the conducting tip. In the other systems this effect is effectively compensated by the alternating ion species. As in the previous system, the image force does feel the difference between one side of the step and the other; this is manifested in the opposition of the interactions at either side of the step. Over the Cl ion the image force is attractive and over the Na ion the force is repulsive. This is a reflection of the image charge distribution produced in the tip by the charged step system, an exaggerated version of the effect seen over the vacancy. The significance of the image force above the ions of the charged step is in agreement with our preliminary results of Ref. [12], where it was found that the image force is very sensitive to the charge of the system between the electrodes.

4. Discussion

In this paper we considered the contributions to the force acting on a tip in a typical setup of an NC-SFM, including: (i) a macroscopic van der Waals interaction between the macroscopic tip and substrate that is always attractive and gives no image contrast; (ii) a microscopic force between the tip apex and the sample that we described using the shell model; for the first time (iii) the image interaction due to macroscopic polarisation of the metal electrodes (both tip and substrate). The latter two contributions may be either attractive or repulsive depending on the distance to the surface and the nature of the surface site that the tip is above. They both play a role in image contrast in the NC-SFM experiment. We clearly demonstrated in this paper the significance of the image interaction, which in some cases is the dominant force. It is especially interesting to note the ability of the image force to resolve the charged di-vacancy and charged step. This shows that the image force could be the dominant source of contrast in NC-AFM images of charged features.

In this study we have adopted several approximations that we are now going to discuss. First, note that we have assumed a particular setup for our model, in terms of the way the bias is applied to the system, as can be seen in Fig. 1. This type of setup is commonly used [35], but other possibilities may exist. For example, a setup where the tip and substrate are decoupled and their potentials are changed independently is equivalent, since only the absolute magnitude of the potential difference between the tip and the metal substrate matters.

Another limitation of the present model is that, for the calculation of the image interaction, we studied finite clusters of a particular shape. However, it is important to understand how the result of the calculation would depend on the size of the cluster if we wish to make any general conclusions about image forces in these systems. As has been mentioned in previous sections, the image force over a particular ion is somewhat

dependent on the geometry of the system being studied. Note that we cannot increase the cluster size indefinitely, since it is limited to roughly twice the radius of the sphere used to model the tip. Beyond this limit the top of the sphere affects the interaction with the surface; this is an unphysical result as, in reality, the tip has essentially infinite height at this scale. In order to investigate the effect of the size of the cluster, we calculated the image force over the same terrace Na ion as in the first system studied, but increased the size of the cluster by several hundred atoms (being still within the limit of the maximum cluster size). This effectively means that the local geometry and charge environment of the ion under the tip apex remain the same, but the total number of charges in the system changes significantly. The calculations show that the image force over the cluster does increase as the number of atoms is increased, but then converges. The increase in image force is due to the interactions of the extra charges in the system, but the difference is an order of magnitude smaller than the image force itself and so would not affect our results significantly.

For consistency, throughout this study we have used a neutral nano-tip. It is known, however, that the tips used in real experiments can be highly contaminated by external material, which may lead to tip charging. Therefore, it is relevant to study the effect of a charged tip (i.e. a nano-tip with a different number of anions and cations) on the image force. To simulate this, we added four uncompensated oxygen ions to the original nano-tip so that its net charge became $-8e$. We found that the image force more than doubles over the charged step. This system is an extreme example of this effect, but an increase in image force can be seen when using a charged tip in all the systems that have been studied here. The effects of tip contamination could be even more significant in the case of contact SFM. In previous studies of contact SFM imaging [36], the importance of ion displacements and ion exchange between tip and surface has been demonstrated. Our results here show that displacement of ions causes a large increase in the image force between the tip and surface. Ion exchange may also charge the tip, again changing the image force. This means that the image force could exaggerate the effects of ion displacement on imaging of conducting materials or thin films with contact AFM.

The image force also depends on the charge distribution and ionicity of the nano-tip used, as well as the charge itself. As has been discussed in our recent paper [37], a more realistic model of an NC-SFM tip would probably consist of an ionic oxide layer covering a semiconducting silicon tip. The simplest model of this tip is an oxygen atom or a hydroxyl group adsorbed on a silicon cluster [37]. This model represents a nano-tip with a decaying ionicity as you move away from the apex. The reduction of the magnitude of the charges in the nano-tip would reduce the magnitude of the image charges in the conducting tip and, therefore, the image force.

Acknowledgements

LNK and ASF are supported by EPSRC. We are grateful to A. Baratoff, R. Bennewitz, E. Meyer and A.I. Livshits for useful discussions and to A.L. Rohl for help in MARVIN calculations.

Appendix A

In this appendix we show explicitly that the function $\phi_{\mathrm{ind}}(\boldsymbol{r}_A, \boldsymbol{r}_B)$ of Eq. (8) is symmetric with respect to its variables. First of all, one has to be clear about the notation. While considering the function $\phi_{\mathrm{ind}}(\boldsymbol{r}_A, \boldsymbol{r}_B)$, we imply that the polarising unit charge is located at $\boldsymbol{r}_B$ and, therefore, all image charges and their positions entering Eq. (8) will be designated by the letter B, e.g. $\zeta_k(B)$, $\xi_k(B)$, $\boldsymbol{r}_{\xi_k}(B)$, etc. Consequently, while considering the function $\phi_{\mathrm{ind}}(\boldsymbol{r}_B, \boldsymbol{r}_A)$ we imply that the source unit charge is at $\boldsymbol{r}_A$ and the image charges and their positions will be marked by the letter A, e.g. $\xi_k(A)$, $\boldsymbol{r}_{\xi_k}(A)$.

Let us now write down separately Eq. (8) for $\phi_{\mathrm{ind}}(\boldsymbol{r}_A, \boldsymbol{r}_B)$ and $\phi_{\mathrm{ind}}(\boldsymbol{r}_B, \boldsymbol{r}_A)$ and compare them term by term. For simplicity we assume that the expansions are infinite. The first terms in both expressions are obviously identical since $|\boldsymbol{r}_A - \hat{\sigma}\boldsymbol{r}_B| = |\boldsymbol{r}_B - \hat{\sigma}\boldsymbol{r}_A|$. Let us now prove that the first terms in

the first sum in both expansions are also identical term by term, i.e. that for any k

$$\frac{\xi_{k+1}(A)}{|\boldsymbol{r}_B-\boldsymbol{r}_{\xi_{k+1}}(A)|}=\frac{\xi_{k+1}(B)}{|\boldsymbol{r}_A-\boldsymbol{r}_{\xi_{k+1}}(B)|}. \tag{14}$$

First of all, a direct calculation shows that they are identical for $k=0$, which can be written down in a symbolic form as

$$\frac{\chi(\boldsymbol{x})}{|\boldsymbol{y}-\boldsymbol{f}(\boldsymbol{x})|}=\frac{\chi(\boldsymbol{y})}{|\boldsymbol{x}-\boldsymbol{f}(\boldsymbol{y})|}, \tag{15}$$

where $\chi(\boldsymbol{r})=-R/|\boldsymbol{r}-\boldsymbol{R}_s|$ and the function $\boldsymbol{f}(\boldsymbol{r})$ has been introduced in Eq. (7). It is implied in the above identity that $\boldsymbol{x}=\boldsymbol{r}_A$ and $\boldsymbol{y}=\boldsymbol{r}_B$; however, it obviously holds for *any* choice of vectors $\boldsymbol{x}$ and $\boldsymbol{y}$. Note that this result simply corresponds to the case of a single sphere for which the potential $\phi_{\mathrm{ind}}(\boldsymbol{r}_A,\boldsymbol{r}_B)$ is known to be symmetric [18]. Consider now the case of any k. Let us denote $\rho_A^{(n)}=\hat{\sigma}\boldsymbol{r}_{\xi_n}(A)$ and $\rho_B^{(n)}=\hat{\sigma}\boldsymbol{r}_{\xi_n}(B)$ for $\forall n=1,2,\ldots$. Then it follows from Eq. (7) that $\boldsymbol{r}_{\xi_{n+1}}(A)=\boldsymbol{f}[\rho_A^{(n)}]$ and $\rho_A^{(n+1)}=\hat{\sigma}\boldsymbol{f}[\rho_A^{(n+1)}]$ for any $n\geq 1$ [while $\boldsymbol{r}_{\xi_1}(A)=\boldsymbol{f}(\boldsymbol{r}_A)$ and $\rho_A^{(0)}=\boldsymbol{r}_A$ for $n=0$]; similar formulae can be written for the charges generated by the source unit charges at $\boldsymbol{r}_B$. Using this notation, we have $\xi_k(A)=(-1)^k\chi(\boldsymbol{r}_A)\chi[\rho_A^{(1)}]\ldots\chi[\rho_A^{(k)}]$ and the same for $\xi_k(B)$, so that Eq. (14) can be rewritten as:

$$\chi(\boldsymbol{r}_A)\chi[\rho_A^{(1)}]\cdots\chi[\rho_A^{(k-1)}]\left\{\frac{\chi[\rho_A^{(k)}]}{|\boldsymbol{r}_B-\boldsymbol{f}[\rho_A^{(k)}]|}\right\}$$
$$=\chi(\boldsymbol{r}_B)\chi[\rho_B^{(1)}]\cdots\chi[\rho_B^{(k-1)}]\left\{\frac{\chi[\rho_B^{(k)}]}{|\boldsymbol{r}_A-\boldsymbol{f}[\rho_B^{(k)}]|}\right\}. \tag{16}$$

The expressions in the square brackets in either side of Eq. (16) can be simplified by means of the identity in Eq. (15). Namely, we use $\boldsymbol{x}=\rho_A^{(k)}$ and $\boldsymbol{y}=\boldsymbol{r}_B$ to simplify the expression in the square brackets in the left hand side of Eq. (16) and $\boldsymbol{x}=\rho_B^{(k)}$ and $\boldsymbol{y}=\boldsymbol{r}_A$ in the right-hand side, giving

$$\chi(\boldsymbol{r}_A)\chi[\rho_A^{(1)}]\cdots\chi[\rho_A^{(k-1)}]\left[\frac{\chi(\boldsymbol{r}_B)}{|\rho_A^{(k)}-\boldsymbol{f}(\boldsymbol{r}_B)|}\right]$$
$$=\chi(\boldsymbol{r}_B)\chi[\rho_B^{(1)}]\cdots\chi[\rho_B^{(k-1)}]\left[\frac{\chi(\boldsymbol{r}_A)}{|\rho_B^{(k)}-\boldsymbol{f}(\boldsymbol{r}_A)|}\right]. \tag{17}$$

Then, we notice that the denominator in the left-hand side can be transformed as follows: $|\rho_A^{(k)}-\boldsymbol{f}(\boldsymbol{r}_B)|=|\boldsymbol{f}(\rho_A^{(k-1)})-\hat{\sigma}\boldsymbol{f}(\boldsymbol{r}_B)|=|\boldsymbol{f}[\rho_A^{(k-1)}]-\rho_B^{(1)}|$ and similarly for the denominator in the right-hand side. In addition, the product $\chi(\boldsymbol{r}_A)\chi(\boldsymbol{r}_B)$ is cancelled out on both sides, so that we are left with:

$$\chi[\rho_A^{(1)}]\cdots\chi[\rho_A^{(k-2)}]\left\{\frac{\chi[\rho_A^{(k-1)}]}{|\rho_B^{(1)}-\boldsymbol{f}[\rho_A^{(k-1)}]|}\right\}$$
$$=\chi[\rho_B^{(1)}]\cdots\chi[\rho_B^{(k-2)}]\left\{\frac{\chi[\rho_B^{(k-1)}]}{|\rho_A^{(1)}-\boldsymbol{f}[\rho_B^{(k-1)}]|}\right\}. \tag{18}$$

Notice that the expression obtained is similar to Eq. (16) with $\boldsymbol{r}_B\to\rho_B^{(1)}$ and $\boldsymbol{r}_A\to\rho_A^{(1)}$and the order k reduced by one. Repeating the procedure, we reduce the order again and get Eq. (18) with $\rho_B^{(1)}\to\rho_B^{(2)}$ and $\rho_A^{(1)}\to\rho_A^{(2)}$. If $k=2p$ is even, this process is repeated until we get exactly Eq. (15) with $\boldsymbol{x}=\rho_A^{(p)}$ and $\boldsymbol{y}=\rho_B^{(p)}$, which is true. If $k=2p+1$ is odd, however, then we will get the same expression $|\rho_B^{(p+1)}=\boldsymbol{f}[\rho_A^{(p)}]\|^{-1}$ on both sides. Thus, Eq. (14) is proven $\forall k$ so that the first terms in the first sum in Eq. (8) are identical in the two expansions. Note again that Eq. (14) is valid for *any* two vectors $\boldsymbol{r}_A$ and $\boldsymbol{r}_B$.

Compare now the second term in the first sum in the expansion of $\phi_{\mathrm{ind}}(\boldsymbol{r}_A,\boldsymbol{r}_B)$ with the first term in the second sum in the expansion of $\phi_{\mathrm{ind}}(\boldsymbol{r}_B,\boldsymbol{r}_A)$, see Eq. (8). They are identical as well for any k, term by term:

$$\frac{-\xi_{k+1}(B)}{|\boldsymbol{r}_A-\hat{\sigma}\boldsymbol{r}_{\xi_{k+1}}(B)|}=\frac{\zeta_{k+1}(A)}{|\boldsymbol{r}_B-\boldsymbol{r}_{\zeta_{k+1}}(A)|}. \tag{19}$$

Indeed, by construction, the image charges $\xi_k(A)$ are built due to the positive source unit charge at $\boldsymbol{r}_A$, whereas the image charges $\zeta_k(A)$ are built due to the source negative unit charge at $\boldsymbol{r}_{\bar{A}}=\hat{\sigma}\boldsymbol{r}_A$, so that $\zeta_k(A)\equiv-\xi_k(\bar{A})$ and $\boldsymbol{r}_{\zeta_k}(A)\equiv\boldsymbol{r}_{\xi_k}(\bar{A})$. Therefore, Eq. (19) appears to be exactly the same as Eq. (14) corresponding to one of the source charges at $\boldsymbol{r}_{\bar{A}}$ rather than at $\boldsymbol{r}_A$. This also means that the second term in the first sum in the expansion of $\phi_{\mathrm{ind}}(\boldsymbol{r}_B,\boldsymbol{r}_A)$ is, term by term, identical to the first term in the second sum in the expansion of $\phi_{\mathrm{ind}}(\boldsymbol{r}_A,\boldsymbol{r}_B)$. Similarly, one can prove that the second terms in the second sum of the two expan-

sions also coincide term by term. The proof is complete.

Appendix B

In this appendix we explain how the contribution $-(\partial U_{\rm el}/\partial z_{\rm s})$ to the total force acting on the tip is calculated. The electrostatic energy $U_{\rm el}$ is given by Eqs. (2), (6) and (8). As has been already mentioned in Section 2, the calculation of the derivative is not simple since the dependence of $U_{\rm el}$ on $z_{\rm s}$ is not only explicit but also contains some implicit dependencies. It is the purpose of this appendix to consider how this derivative is calculated in some detail.

The energy $U_{\rm el}$ consists of two parts: that due to bare electrodes and that due to charges. We first of all consider the first part, i.e. the derivatives with respect to $z_{\rm s}$ of the charge $Q^{(0)}$ and the potential $\phi^{(0)}(\boldsymbol{r})$. Using definitions of charges ς_k given in Section 2.2, one has the following set of recurrent equations for the derivatives of the charges with respect to $z_{\rm s}$:

$$\frac{\partial \varsigma_{k+1}}{\partial z_{\rm s}} = \frac{1}{D_k}\left(\frac{\partial \varsigma_k}{\partial z_{\rm s}} - \frac{\varsigma_k}{D_k}\frac{\partial D_k}{\partial z_{\rm s}}\right),$$

where $\partial_{\varsigma_1}/\partial z_{\rm s}=0$ and the derivatives $\partial D_k/\partial z_{\rm s}$ are in turn obtained from $\partial D_{k+1}/\partial z_{\rm s}=(2/R)+[D_k^{-2}(\partial D_k/\partial z_{\rm s})]$, which starts from $\partial D_1/\partial z_{\rm s}=2/R$. The position of image charges z_k also depend on $z_{\rm s}$ and the corresponding derivatives are easily expressed via the derivatives $\partial D_{\rm k}/\partial z_{\rm s}$ as follows: $\partial z_k/\partial z_{\rm s}=R(\partial D_k/\partial z_{\rm s})-1$. The calculation of the derivative of ς_∞ and z_∞ with respect to $z_{\rm s}$ is calculated easily owing to their explicit dependence on it (see Section 2.2). Thus, the calculation proceeds as follows. First of all, the derivatives $\partial D_k/\partial z_{\rm s}$ for all needed values of $k\le k_0$ are calculated using the recurrent relations above, then the derivatives of the charges and their positions are also calculated. This makes it possible to calculate the derivatives of $Q^{(0)}$ and $\phi^{(0)}(\boldsymbol{r})$ with respect to $z_{\rm s}$ in a simple fashion in accordance with Eqs. (6) and (5).

The calculation of the derivatives of the second part of the energy that is to do with charges $\{q_i\}$ proceeds in a similar manner, although the calculation is more cumbersome. We need the derivatives with respect to $z_{\rm s}$ of the induced potential, $\phi_{\rm ind}(\boldsymbol{r}_j, \boldsymbol{r}_i)$. It follows from Eq. (8) that for every charge q_i we should, therefore, consider the derivatives of the charges ξ_k, ξ'_k as well as of their positions $\boldsymbol{r}_{\xi_k}$ and $\hat{\sigma}\boldsymbol{r}_{\xi_k}$; after that, the same calculation should be repeated for the ζ-sequence. Note that the actual dependence on $z_{\rm s}$ comes from $\boldsymbol{r}_{\rm s}=(0, 0, z_{\rm s})$ in Eq. (7). Let us fix some charge q_i. We first define the derivatives

$$\Gamma_\alpha^{(\xi_k)} = \frac{\partial r_{\xi_k}\alpha}{\partial z_{\rm s}}, \tag{20}$$

where Greek indices α, β will be used to designate the Cartesian components of vectors. Using Eq. (7) one can get the following recurrent relations for the quantities $\Gamma_\alpha^{(\xi_k)}$:

$$\Gamma_\alpha^{(\xi_{k+1})} = \delta_{\alpha z} + \frac{R^2}{R_k^2}\left\{[\theta_\alpha\Gamma_\alpha^{(\xi_k)} - \delta_{\alpha z}] - \frac{2}{R_k^2}\sum_\beta [\theta_\beta\Gamma_\beta^{(\xi_k)} - \delta_{\beta z}]R_{k\alpha}R_{k\beta}\right\}, \tag{21}$$

where the vectors $\boldsymbol{R}_k = \hat{\sigma}\boldsymbol{r}_{\xi_k} - \boldsymbol{R}_{\rm s}$, $\delta_{\alpha\beta}$ is Kronecker's delta symbol and we also defined θ_α as $\theta_\alpha=1$ for $\alpha=x, y$ and $\theta_z=-1$. Note that this relation can be used starting for $k=0$ if we set $\boldsymbol{R}_0=\boldsymbol{r}_i-\boldsymbol{R}_{\rm s}$ and $\Gamma_\alpha^{(\xi_0)}=0$.

Finally, the derivatives of the charges ξ_k can be calculated using their definition in Eq. (7) and the quantities in Eq. (20) as follows:

$$\frac{\partial \xi_{k+1}}{\partial z_{\rm s}} = \frac{R}{R_k}\left\{\frac{\partial \xi_k}{\partial z_{\rm s}} - \frac{\xi_k}{R_k^2}\sum_\beta [\theta_\beta\Gamma_\beta^{(\xi_k)} - \delta\beta z]R_{k\beta}\right\}, \tag{22}$$

where again this expression can be used starting from $k=0$ if we set: $\partial\xi_0/\partial z_{\rm s}=-1$. First, one calculates the derivatives $\Gamma_\alpha^{(\xi_k)}$ using the recurrent equations in Eq. (21); then the derivatives of the charges ξ_k are easily calculated from Eq. (22). Then this procedure is repeated for the ζ-sequence.

The formulae obtained above allow one to

calculate the contribution to the force on the tip coming from the induced potential and the induced charge caused by every charge q_i in the system. This calculation proceeds by considering every charge one after another and adding its contribution to the total force. Finally, adding the contribution to the force from the bare electrodes, we get the total electrostatic force, $F_z^{(\mathrm{el})} = -(\mathrm{d}U_{\mathrm{el}}/\mathrm{d}z_{\mathrm{s}})$.

Appendix C

In this appendix we consider the calculation of the contribution to the force acting on some charge q from the electrostatic energy U_{el}. Using Eq. (2), we obtain:

$$F_{i\alpha} = -\frac{\partial U_{\mathrm{el}}}{\partial r_{i\alpha}} = -q_i \frac{\partial \phi^{(0)}(\boldsymbol{r}_i)}{\partial r_{i\alpha}} - q_i \tfrac{1}{2} \sum_j q_j \left[\frac{\partial \phi_{\mathrm{ind}}(\boldsymbol{r}_i, \boldsymbol{r}_j)}{\partial r_{i\alpha}} + \frac{\partial \phi_{\mathrm{ind}}(\boldsymbol{r}_j, \boldsymbol{r}_i)}{\partial r_{i\alpha}} \right], \tag{23}$$

where Greek index α is used for Cartesian components of vectors. Several terms emerge here. The derivative of the potential $\phi^{(0)}(\boldsymbol{r}_i)$ defined by Eq. (5) is straightforward, since the positions of the charges ς_k depend only on the position z_{s} of the sphere. The same is also true for the derivative $\partial\phi_{\mathrm{ind}}(\boldsymbol{r}_i, \boldsymbol{r}_j)/\partial r_{i\alpha}$ taken with respect to the first (explicit) variable of the induced potential, so that this derivative is calculated directly using Eq. (8) with respect to the first argument and then setting $\boldsymbol{r}$ to $\boldsymbol{r}_i$. The calculation of the other derivative, $\partial\phi_{\mathrm{ind}}(\boldsymbol{r}_j, \boldsymbol{r}_i)/\partial r_{i\alpha}$, is trickier and requires some subtle consideration similar to that of Appendix B. This leads to a set of recurrence relations for the derivatives of image charges and their positions. This difficulty, however, can be easily overcome by recalling that the function $\phi_{\mathrm{ind}}(\boldsymbol{r}_i, \boldsymbol{r}_j)$ is symmetric with respect to the permutation of its variables (Appendix A). Finally, we have

$$F_{i\alpha} = -q_i \left[\frac{\partial \phi^{(0)}(\boldsymbol{r}_i)}{\partial r_{i\alpha}} + \sum_j q_j \frac{\partial \phi_{\mathrm{ind}}(\boldsymbol{r}_i, \boldsymbol{r}_j)}{\partial r_{i\alpha}} \right] = -q_i \frac{\partial \phi_{\mathrm{ind}}(\boldsymbol{r}_i)}{\partial r_{i\alpha}}. \tag{24}$$

References

[1] N. Burnham, R. Colton, H. Pollock, Nanotechnology 4 (1993) 64.
[2] R.E. Egdell, F.H. Jones, J. Mater. Chem. 8 (1998) 469.
[3] W. Hebenstreit, J. Redinger, Z. Horozova, M. Schmid, R. Podloucky, P. Varga, Surf. Sci. 424 (1999) L321.
[4] K. Fukui, H. Onishi, Y. Iwasawa, Phys. Rev. Lett. 79 (1997) 4202.
[5] M. Guggisberg, M. Bammerlin, R. Lüthi, C. Loppacher, F. Battiston, J. Lü, A. Baratoff, E. Meyer, H.-J. Güntherodt, Appl. Phys. A 66 (1998) S245.
[6] S. Morita (Ed.), Proceedings of the First International Workshop on Noncontact Atomic force Microscopy, Appl. Surf. Sci. 140 (1999).
[7] F.J. Giessibl, Science 267 (1995) 68.
[8] A.I. Livshits, A.L. Shluger, A.L. Rohl, A.S. Foster, Phys. Rev. B 59 (1998) 2436.
[9] M. Bammerlin, R. Lüthi, E. Meyer, J. Lü, M. Guggisberg, C. Loppacher, C. Gerber, H.J. Güntherodt, Appl. Phys. A 66 (1998) S293.
[10] R. Bennewitz, M. Bammerlin, M. Guggisberg, C. Loppacqher, A. Baratoff, E. Meyer, H.-J. Güntherodt, Surf. Interface Anal 27 (1999) 462.
[11] C. Loppacher, M. Bammerlin, M. Guggisberg, F. Battiston, R. Benewitz, S. Rast, A. Baratoff, E. Meyer, H.-J. Güntherodt, Appl. Surf. Sci. 140 (1999) 287.
[12] L.N. Kantorovich, A.I. Livshits, A.M. Stoneham, J. Phys.: Condens. Matter (1999) submitted for publication.
[13] M.W. Finnis, Surf. Sci. 241 (1991) 61.
[14] M.W. Finnis, R. Kaschner, C. Kruse, J. Furthmüller, M. Scheffler, J. Phys. Condens. Matter 7 (1995) 2001.
[15] M. García-Hernández, P.S. Bagus, F. Illas, Surf. Sci. 409 (1998) 69.
[16] D.M. Duffy, J.H. Harding, A.M. Stoneham, Philos. Mag. 67 (1993) 865.
[17] L.D. Landau, E.M. Lifshitz, L.P. Pitaevskii, Electrodynamics of Continuous Media vol. 8 Pergamon, Oxford, 1993.
[18] J.D. Jackson, Classical Electrodynamics, Wiley, New York, 1999.
[19] W.R. Smythe, Static and Dynamic Electricity, McGraw-Hill, New York, 1968.
[20] M.J. Hagmann, Int. J. Quant. Chem.: (Symp.) 28 (1994) 271.
[21] J.G. Simmons, J. Appl. Phys. 35 (1964) 2472.
[22] H.Q. Nguyen, P.H. Cutler, T.E. Feuchtwang, N. Miskovsky, A.A. Lucas, Surf. Sci. 160 (1985) 331.
[23] L.-H. Pan, T.E. Sullivan, V.J. Peridier, P.H. Cutler, N.M. Miskovsky, Appl. Phys. Lett. 65 (1994) 2151.
[24] H. Morawitz, I.P. Batra, R. Reinisch, G.R. Henry, Surf. Sci. 180 (1987) 333.
[25] J. Bono, R.H. Good, Surf. Sci. 151 (1985) 543.
[26] A.A. Lucas, J.P. Vigneron, J. Bono, P.H. Cutler, T.E. Feuchtwang, R.H. Good, Z. Huang, J. Phys. (Paris) Colloq. 45 (1984) C9.

[27] C. Argento, R.H. French, J. Appl. Phys. 80 (1996) 6081.
[28] D. Gay, A. Rohl, J. Chem. Soc. Faraday Trans. 91 (1995) 925.
[29] A. Shluger, A. Rohl, D. Gay, R. Williams, J. Phys. Condens. Matter 6 (1994) 1825.
[30] B.G. Dick, A.W. Overhauser, Phys. Rev. 112 (1958) 603.
[31] R. Grimes, C. Catlow, A. Stoneham, J. Phys. Condens. Matter 1 (1989) 7367.
[32] R.H. French, R.M. Cannon, L.K. DeNoyer, Y.-M. Chiang, Solid State Ionics 75 (1995) 13.
[33] A.L. Shluger, L.N. Kantorovich, A.I. Livshits, M.J. Gillan, Phys. Rev. B 56 (1997) 15 332.
[34] K. Fukui, H. Onishi, Y. Iwasawa, Phys. Rev. Lett. 79 (1997) 4202.
[35] H. Tomiye, H. Kawami, M. Izawa, M. Yosyhimura, T. Yao, Jpn. J. Appl. Phys. 34 (1995) 3376.
[36] A.I. Livshits, A.L. Shluger, Faraday Discuss. 106 (1997) 425.
[37] P. Susko, A. Foster, L. Kantorovich, A. Shluger, Appl. Surf. Sci. 144–145 (1999) 608.